

# UV-curable silicone materials with tuneable mechanical properties for 3D printing



Aleksandra Foerster<sup>a,1</sup>, Vinotharan Annarasa<sup>b,1</sup>, Anna Terry<sup>c</sup>, Ricky Wildman<sup>a</sup>, Richard Hague<sup>a</sup>, Derek Irvine<sup>b</sup>, Davide S.A. De Focatiis<sup>b</sup>, Christopher Tuck<sup>a,\*</sup>

<sup>a</sup>Centre for Additive Manufacturing, University of Nottingham, Nottingham NG8 1BB, United Kingdom

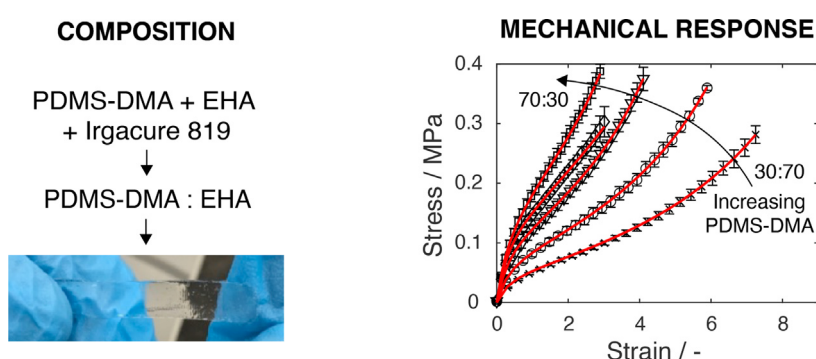
<sup>b</sup>Faculty of Engineering, University of Nottingham, Nottingham, NG7 2RD, United Kingdom

<sup>c</sup>AWE, Aldermaston, Reading, RG7 4PR, United Kingdom

## HIGHLIGHTS

- Novel UV-curable, highly flexible silicone compositions which are suitable for use in a valve-based jetting process were developed.
- Developed materials were characterised using FTIR, DSC, TGA and uniaxial tensile tests.
- It was shown that the mechanical properties were strongly dependent on the composition and that the stiffness could be made to vary from ~50 kPa to ~180 kPa.
- An EV model demonstrated a growth in the network density and a drop in the limiting extensibility with increasing silicone content.

## GRAPHICAL ABSTRACT



## ARTICLE INFO

### Article history:

Received 9 December 2020

Revised 4 March 2021

Accepted 24 March 2021

Available online 30 March 2021

### Keywords:

Silicone

Material Jetting

UV-curable

Mechanical properties tunability

## ABSTRACT

In this paper, we present the development of a family of novel, UV-curable, highly flexible, 3D printable silicone-based materials, the mechanical properties of which can be tuned simply by varying the ratio of the polymerisable reagents within the formulation. This tuneability is achieved by exploiting the balance between in-cure phase separation and differential reactivity within the formulation to successfully produce composite structures *via* both casting and valve-based jetting processes. The structure and properties of both cast and 3D printed materials were examined in a range of compositions of silicone to acrylate between 30:70 and 70:30. The phase segregated structure, evidenced from distinct glass transitions, and the thermal stability of these materials were both shown to be insensitive to the composition ratio, whereas the elastic properties were strongly dependent on the composition. The stiffness could be made to vary from ~50 kPa to ~180 kPa by increasing the silicone content. This study will guide the formation of a new generation of Additive Manufacturing (AM) silicone elastomeric functional structures for various applications ranging from flexible electronics to regenerative medicine, which will benefit from local changes in mechanical properties within the same material family.

Crown Copyright © 2021 Published by Elsevier Ltd. This is an open access article under the CC BY license (<http://creativecommons.org/licenses/by/4.0/>).

\* Corresponding author.

E-mail address: [Christopher.Tuck@nottingham.ac.uk](mailto:Christopher.Tuck@nottingham.ac.uk) (C. Tuck).

<sup>1</sup> These authors contributed equally to this work.

## 1. Introduction

Silicone elastomers are members of the organosilicone family of compounds and can be obtained *via* crosslinking functionalised polydimethylsiloxane (PDMS) at either elevated temperatures or at room temperature. The most common silicones used in AM are the room temperature cured silicones which utilize one of three curing reactions: (a) hydrosilation reaction in the presence of catalyst (addition cure system), (b) moisture curing reaction (condensation cure system), or (c) photopolymerisation in the presence of photoinitiator (UV cure system). The chemical structure and material properties of silicone elastomers make them useful in a wide variety of applications, and depending on which mechanical properties are of interests, different silicone formulations are used. In applications such as automotive, electronics, energy absorbers or thermal insulation [1–3], where stiff materials are required, silicones with high molecular weight which can be crosslinked in the presence of a platinum catalyst are used, and very often high surface area silica are added as a reinforcement agent [4]. For applications such as soft robotics [5], biomedical devices [6] and stretchable electronics [7], softer platinum-free formulations, void of silica, have been developed [8]. A range of soft silicones, thermoplastics [9] and thermosets [10], have been reported, including self-healing dielectric elastomers [11].

Recent developments in Additive Manufacturing (AM) technology have delivered the potential to fabricate components with complex, detailed and precise structures, thereby broadening the range of applications for various materials [12–15]. Thus, AM is becoming a viable alternative to traditional moulding techniques commonly used for silicone materials [16–19]. In practice, the principal AM technique capable of handling highly viscous fluids, such as silicones, is material extrusion [20–27]. However, the relatively limited complexity of the parts that can be produced with this technique and its low production efficiency present significant limitations. Alternative methods such as Freeform Reversible Embedding (FRE) offer contact-based support-free solutions for the 3D printing of silicone [28]. Although FRE produces uniform, high-quality silicone features, its low throughput limits industrial use and its contact-based nature requires extensive and complex planning strategies.

In addition to material extrusion, a variant of the Material Jetting method, known as “valve-based” jetting, also enables the processing of high viscosity materials and feedstocks. Valve-based jetting can offer both high resolution and a relatively high throughput of material. Compared to the contemporary layer-by-layer AM methodologies such as powder bed fusion that enable complex geometries associated with AM, material jetting offers the ability to co-deposit materials within a pre-defined voxel pattern [19,20] thanks to the potential of using multiple heads. Valve-based jetting differs from traditional material jetting that uses thermal [29] or piezo-electric [30] inkjet heads by using micro-dispensing valves [31], that work on a combination of pneumatic and mechanical actuation. This allows discrete volumes (nl) of viscous fluids to be dispensed on demand. In our previous work, we have shown that high viscosity silicones can be processed with this technique and that latticed silicone structures can be successfully fabricated [31,32]. The technique has seen some commercialisation recently through Wacker with a similar technique for printing high viscosity materials [33].

Despite progress high viscosity valve-based jetting there has been limited activities on the development of silicone materials specifically for jetting methods. Studies focused on the viscoelastic properties of printable silicones [34,35], their mechanical properties [36] or biocompatibility [37] are available. However, these studies are on modified commercial formulations and do not inves-

tigate compatibility between the material and processing method and the consequent impact on component properties.

Silicones compatible with various AM methods have been reported to be two-part, temperature cured systems [22,24,38] and single component UV curables [39–41]. The advantage of using UV light to cure materials during printing surrounds the reduced printing time due to faster droplet pinning [42]. There are various formulations of UV-curable silicones with potential for AM [28,34–36,43]. However, it is difficult to either adjust the chemical properties to tailor the final mechanical performance of the constructed device for a given application, and/or achieve the rheological properties appropriate for inkjet or valve-based printing. Therefore, developing a printable silicone formulation with easily tuneable mechanical properties would broaden their adoption within the AM community and beyond, accelerating adoption of AM technology and realising new innovative products based on material and design complexity.

Here we present novel UV curable silicone elastomers which successfully exhibit both the rheological properties for valve-based jetting and tuneable mechanical properties when part of the final desired structure. Furthermore, we demonstrate that this material property control is predictable by simply changing the ratio between the acrylate and silicone components within the structure. The influence of the silicone to acrylate ratio on curing behaviour, structural characteristics, and thermal properties are also reported, and linked to the macro material behaviour. Additionally, a hyperelastic rubber material model [44] was fitted to the mechanical data to understand the influence of composition on the crosslinked network achieved during cure.

## 2. Materials and methods

### 2.1. Materials

Di-functional methacryloxypropyl terminated polydimethylsiloxane (PDMS-DMA), mono-functional 2-ethyl hexyl acrylate (EHA) and bis(2,4,6-trimethylbenzoyl)-phenylphosphine oxide (Irgacure 819) were utilised in this work. They were purchased from Gelest, Sigma Aldrich and BASF, respectively. All chemicals were used as received. Typically, silica fillers are incorporated into silicone elastomers as reinforcing agents. In this study silica was not added because of the complexity that would arise, especially in the context of 3D printing.

### 2.2. General procedure for the synthesis of the paste formulations

To develop and synthesise a new UV curable silicone, the appropriate quantity of PDMS-DMA oligomer, with a weight ( $M_w^{\text{-PDMS-DMA}}$ ) and number ( $M_n^{\text{-PDMS-DMA}}$ ) average molecular weight of 47,560 g mol<sup>-1</sup> and 32,560 g mol<sup>-1</sup>, respectively, required to achieve the desired co-monomer ratio was mixed with EHA monomer with molecular weight ( $M^{\text{EHA}}$ ) of 184.27 g mol<sup>-1</sup> and 1 wt% of photoinitiator Irgacure 819 in UV opaque glass. EHA was used as a low molecular weight reactive diluent with an acrylate group available for polymerisation, both with itself and the PDMS-DMA. The PDMS-DMA and EHA were mixed in different weight ratios (30:70, 40:60, 50:50, 60:40, 70:30). Fig. 1 shows the molecular structures of the acrylate monomer, silicone oligomer and the photoinitiator used in the formulations.

For formulation development, reference samples were prepared by transferring 0.3 mL of the ink (with a given ratio) into an aluminium mould of dimensions 1.5 mm × 10 mm × 40 mm and cured for 30 s using a Phoseon's FireEdge FE400 UV LED set at an intensity of 5%. This UV light has a nominal flux density (radiant

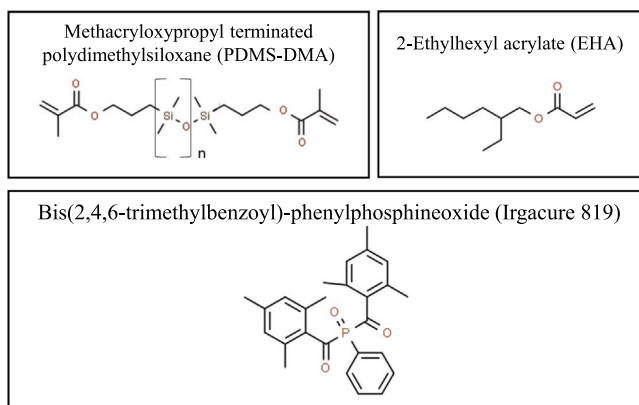


Fig. 1. Molecular structures of the UV curable ink components.

power per unit area) of  $8 \text{ W cm}^{-2}$  at 100% intensity and a wavelength of 395 nm. The FE400 unit is identical to that used in the valve-based jetting system. The distance between the mould and the UV light was  $\sim 10 \text{ mm}$ . The prepared samples were further characterised and mechanically tested.

### 2.3. Formulation characterisation

#### 2.3.1. Molecular characterisation: FTIR

To characterise the chemical properties of formulated and cast silicones samples before and after curing to determine the reduction in the quantity of vinyl groups, FTIR-ATR spectroscopy analysis has been performed. ATR spectra were measured on a Frontier Fourier Transform spectrometer (Perkin Elmer) based on the attenuated total reflection method [45]. Samples were placed directly on the 3 mm in diameter diamond ATR crystal (Pike GladiATR module). Absorption spectra of the samples were recorded at a constant temperature ( $25 \text{ }^\circ\text{C}$ ) in the range  $500\text{--}3500 \text{ cm}^{-1}$ , at a resolution of  $4 \text{ cm}^{-1}$ . A background measurement was run for each sample before its FTIR analysis. The FTIR-ATR spectra were recorded using Spectrum software. A minimum of 3 samples were tested for each uncured and cured composition.

### 2.4. Thermal characterisation

#### 2.4.1. Inks and components

TGA analyses were conducted on the uncured components (PDMS-DMA and EHA) in ceramic vessels with  $\sim 10 \text{ mg}$  mass samples using a TGA TL 9000 (Perkin Elmer). A single sample was

tested in each instance. The experiment was conducted under  $\text{N}_2$  atmosphere (flow of  $20 \text{ mL min}^{-1}$ ) while the heating rate was set to  $40 \text{ }^\circ\text{C min}^{-1}$ .

Samples of the reagents were subjected to photo DSC (DSC 8000/8500, Perkin-Elmer) analysis to study the UV-curing behaviour of the inks, and to examine the degree of monomer conversion during photopolymerisation. The instrument was equipped with an OmniCure 2000 curing system (UV light source) that employed light from a 200 W mercury lamp of 250–450 nm in bandwidth. Approximately 10 mg of ink formulations with different silicone:acrylate ratios were placed into aluminium pans, weighed and positioned into the holder of the instrument at room temperature. A minimum of 3 samples were tested for each composition.

#### 2.4.2. Cured samples

TGA analyses were also conducted on cured and cast samples using the process highlighted above for the uncured components. A single sample was analysed in each instance.

DSC analysis was used to define the glass transition temperatures  $T_g$  of the various cured compositions. They were determined using a Linkam DSC600 in conjunction with the LNP96 liquid nitrogen cooling system. This setup was necessary to achieve a starting temperature of  $-150 \text{ }^\circ\text{C}$ . As this system is a single cell calorimeter, DSC count (proportional to heat flow) is measured. Samples of  $\sim 5 \text{ mg}$  were loaded onto aluminium pans and placed into the crucible. Following a  $\text{N}_2$  purge, the samples were cooled to  $-150 \text{ }^\circ\text{C}$  and subsequently reheated at a rate of  $5 \text{ }^\circ\text{C min}^{-1}$  through to a temperature of  $20 \text{ }^\circ\text{C}$ . A minimum of 3 samples were tested for each composition.

### 2.5. Swelling study

The sol content and swelling fraction were measured by the mass differential after incubation of the polymer network in toluene. Firstly, polymer cubes ( $2 \text{ mm} \times 2 \text{ mm} \times 2 \text{ mm}$ ) were cut from crosslinked cast samples. Subsequently, the cubes were weighed to find the initial mass ( $W_i$ ), and immersed in toluene for 48 h. The samples were then removed from toluene and dried. Having removed any unreacted polymer, the samples were weighed again to determine the dry mass ( $W_d$ ). The sol gel fraction is calculated via [46]:

$$\text{Sol} = \frac{W_i - W_d}{W_i} \quad (1)$$

and the swelling fraction is calculated via [47]:

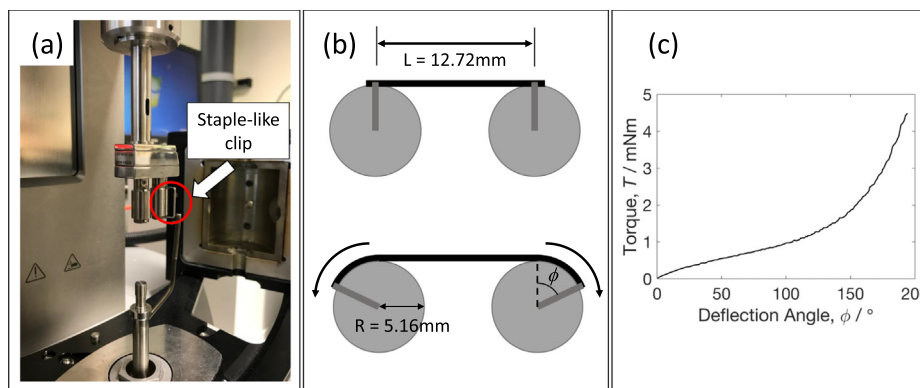


Fig. 2. (a) The experimental setup used for the mechanical tests. One of the clips is left protruding out of the drums for illustration. (b) A schematic of the counter-rotation of the drums with key dimensions, including the drum radius  $R$ , gauge length  $L$  and deflection angle  $\phi$ . (c) A representative example of the raw data obtained from the experiment. This particular data is for a PDMS-DMA:EHA sample with a ratio 70:30 specimen.

$$\text{Swelling} = \frac{W_s - W_d}{W_d} \quad (2)$$

where  $W_s$  is the weight of the polymer sample after swelling.

## 2.6. Mechanical characterisation

Uniaxial tensile tests were conducted using an Anton Paar Rheometer MCR 302 equipped with the Sentmanat Extensional Rheometry (SER3-P) fixture. Cast samples were cut into rectangular bars of dimensions  $\sim 0.35 \text{ mm} \times 5.75 \text{ mm} \times 25 \text{ mm}$  using sharp parallel blades. The samples from the various compositions could be cut easily with the sharp blades, suggesting a low tear strength. A Hildebrand rubber thickness gauge and a calibrated HP Scanjet G4010 were used to measure thickness and width, respectively.

In practice, the process of obtaining the thickness measurement was complicated by the viscoelasticity and high compliance exhibited by the elastomers as the rubber thickness gauge probe applied a small force, causing the material to deform. Therefore, to calculate the thickness in the absence of the probe force, the elastic solution developed by Lebedev and Ufliand was used to correct for the deformation [48].

For tensile testing, rectangular specimens were attached to the drums of the SER3-P apparatus using staple-like clips, strain was applied to the specimen by the counter-rotation of the drums as illustrated by Fig. 2. A small torque of  $10 \mu\text{N}\cdot\text{m}$  was applied to ensure that the specimen was straight prior to the test. The tests were carried out at a rotational speed corresponding to a constant true strain rate  $\dot{\epsilon}_{\text{true}}$  of  $0.1 \text{ s}^{-1}$  at room temperature ( $20 \pm 1 \text{ }^\circ\text{C}$ ).

The raw data obtained from the tests can be utilised to determine the nominal strain  $\epsilon$  and the nominal stress  $\sigma$ . The former is defined as

$$\epsilon = \exp(\dot{\epsilon}_{\text{true}}t) - 1 \quad (3)$$

where  $t$  is the time, and the latter is defined as

$$\sigma = \frac{T}{2awR\lambda\exp(\dot{\epsilon}_{\text{true}}t)} \quad (4)$$

where  $T$  is the torque,  $a$  is the thickness of the specimen,  $w$  is the width of the specimen,  $R$  is the radius of the drums and  $\lambda = (1 + \epsilon)$  is elongation.

## 2.7. General procedure for material jetting

A custom-built apparatus was utilised for the valve-based jetting process. It consisted of a moveable stage which was synchronised with stationary Nordson EFD jetting valves, as presented in [31]. Opening and closing of the nozzle is controlled by a driving pulse as highlighted in Fig. 3. For the purpose of this work, close, pulse and cycle times were  $0.4 \times 10^{-3} \text{ s}$ ,  $0.67 \times 10^{-3} \text{ s}$ , and

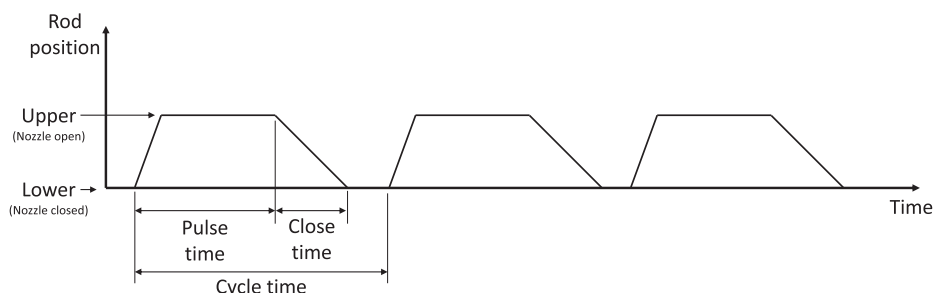


Fig. 3. Schematic of the driving pulse and its effect on the nozzle state. Pulse time is the total time the valve is open, and the cycle time is the total duration of one open/close cycle. Open and close time indicates how fast the valve is open and closed respectively.

$5 \times 10^{-3} \text{ s}$  respectively. These values are user defined and are based on the fluid properties.

During printing, the printhead/substrate standoff distance was  $\sim 1 \text{ mm}$ . The ink was deposited one drop at a time to form a layer, and once a sufficient number of layers are achieved the stage was moved under the FE400 UV LED set at 100% intensity. The distance between the lamp and the printed layer was  $\sim 10 \text{ mm}$ . Droplet spacing, i.e. the distance between adjacent droplets, is an important factor that determines the quality of the printed lines or films and is normally determined by the size of the droplet diameter. Here, continuous printed lines were formed using a  $500 \mu\text{m}$  drop spacing, determined from a droplet diameter of  $600 \mu\text{m}$ . To print and cure a sample  $\sim 0.35 \text{ mm} \times 10 \text{ mm} \times 40 \text{ mm}$  in dimension made up of three layers took roughly one minute (including a  $30 \text{ s}$  cure time). A representative printed PDMS-DMA:EHA sample with a ratio of 70:30 was used for mechanical testing.

## 3. Results and discussion

### 3.1. Molecular structure of silicone using FTIR

UV curable formulations were prepared from the following three main components, (a) a PDMS-DMA oligomer, (b) a reactive EHA monomer, and (c) Irgacure 819 (photoinitiator). The PDMS-DMA forms branching within the 3D cross-linked polymer network, the EHA acts as a diluent and lowers the formulation's viscosity, as well as reducing the branching density; Irgacure 819 is responsible for radical formation by absorbing UV energy.

FTIR analysis was performed both before and after UV polymerisation, to observe the changes in molecular structure that resulted from altering the composition and curing regime. Representative FTIR spectra are highlighted in Fig. 4 for a 50:50 PDMS-

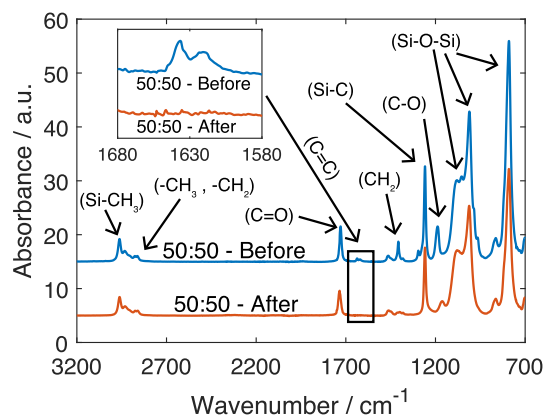


Fig. 4. Representative FTIR spectra of the 50:50 composition before and after UV polymerisation.

DMA:EHA composition. The presence of the characteristic peaks for the silicone species were observed and noted to remain unchanged in intensity post-cure. The stretching vibration ( $\nu_{as}$ ) of the backbone chain of silicone -Si-O-Si groups were observed at 791, 1011, and 1084  $\text{cm}^{-1}$ , the absorption band for the Si-C groups was detected at 1258  $\text{cm}^{-1}$  [49,50], and the presence of Si-CH<sub>3</sub>  $\nu_{as}$  can be seen at 2962  $\text{cm}^{-1}$ . Meanwhile, the absorption band related to the polymerisable methacrylate species were noted to present in the spectrum taken prior to curing only. These peaks are located at 1619  $\text{cm}^{-1}$  and 1636  $\text{cm}^{-1}$  that indicated the presence of the carbon-carbon double bond (C=C) groups, whilst the  $\nu_{as}$  of the C=O group is located at 1730  $\text{cm}^{-1}$ , the peaks corresponding to CH<sub>2</sub> can be seen at 1406  $\text{cm}^{-1}$  and the vibration of the C-O group is observed at 1188  $\text{cm}^{-1}$  [49].

When comparing spectra for the samples before and after UV polymerisation, differences in the absorption peaks at 1406, 1619, 1636  $\text{cm}^{-1}$  were observed. These peaks are all related to the double bond within the methacrylate group, and they were all observed to have significantly decreased after the samples had been cured, which indicated successful UV polymer crosslinking. However, because these peaks have not completely disappeared, it is suggested the reaction did not proceed to completion. The reason for this could be that, as part of the 3D network that is developed, not all of the second functionality of the PDMS-DMA have sufficient flexibility to find and react with another PDMS-DMA group. Similarly, as the network develops, the viscosity of the formulation increases and the diffusion of EHA significantly decreases. Consequently, the probability of encountering unreacted methacrylate groups is reduced.

### 3.2. Swelling study

Fig. 5 presents results from a swelling experiment showing the swelling percentage and sol content within tested formulations. As observed in Fig. 5 the swelling percentage gradually decreased from (992 ± 46) % to (477 ± 39) % as the ratio of the PDMS-DMA:EHA increased from 30:70 to 70:30. This indicates that PDMS-

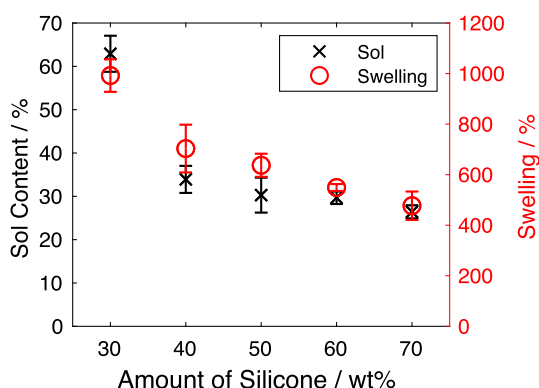


Fig. 5. Degree of swelling and sol content as a function of silicone content.

Table 1

TGA analysis for the sample with various ratios between silicone:acrylate. The I and II peaks refer to the peaks observed in the derivative of the weight loss versus temperature curve, and the weight specified here is the residual weight as shown on Fig. 6.  $T_{95\%}$  is the temperature corresponding to 95% residual weight, or 5% weight loss.

Composition	Weight/%		Temperature/°C		
	I Peak	II Peak	$T_{95\%}$	I Peak	II Peak
30:70	51.5	17.9	343.0	422.0	480.7
40:60	59.8	20.2	351.2	420.3	486.7
50:50	68.1	24.4	356.7	420.0	488.3
60:40	71.8	31.8	355.2	421.3	488.7
70:30	78.9	37.8	363.0	420.0	486.0

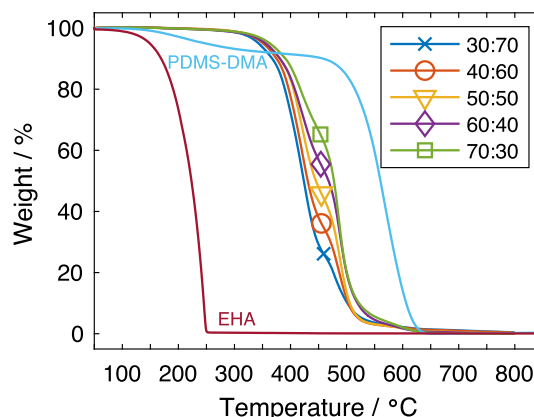


Fig. 6. TGA curves of cured samples prepared with various ratios between silicone:acrylate (30:70, 40:60, 50:50, 60:40 and 70:30), and of the raw components EHA and PDMS-DMA.

DMA contributes to the crosslinking of the network. As illustrated in Fig. 5, the sol content of cured polymer samples was reduced from (62 ± 3) % to (26 ± 1) % as the ratio of PDMS-DMA:EHA increased from 30:70 to 70:30.

### 3.3. Thermal analysis

Thermogravimetric analysis (TGA) was conducted to study the thermal stability of the silicone samples prepared with different ratios of reagents. The TGA results are shown in Fig. 6 and the degradation temperature, which is defined as the temperature at the peak of the derivative of weight loss vs temperature, is listed for all the samples in Table 1. The derivative weight loss vs temperature plots, for all compositions considered, have been provided in the supplementary material, see Fig. S1-S5.

As can be observed in Fig. 6, the degradation of EHA monomer occurs below 200 °C while the dominant degradation step for unreacted PDMS-DMA starts at around 390 °C which corresponds to the split of Si-CH<sub>3</sub> bonds, followed by complete loss of pure PDMS-DMA above 540 °C [42]. The weight loss observed in the initial stage before 390 °C is most likely related to the small percentage of low oligomer molecular weight present in the PDMS-DMA. Once PDMS-DMA is mixed with EHA, and the mixture is cured, the degradation temperature is seen to increase when compared to pure EHA, suggesting the formation of cross-links between the components. The cross-linked polymers decompose in two stages. The mass loss of the cross-linked samples differs depending on the ratio between silicone and acrylate (Table 1). A higher proportion of the mass was lost at the second peak temperature when more silicone was present in the composition.

It was reported by Oglioni *et al.* [51] that the thermal degradation behavior of silicone elastomers obtained via a hydrosilylation reaction between the vinyl-terminated polydimethylsiloxane and the hydride-functional crosslinker is affected strongly by the stoi-

chiometry of the network reactant and the degree of crosslinking. In the photopolymerised materials used in the current work, the characteristic peak temperatures are observed to be similar for all compositions. The first peak can be seen around  $\sim 420$  °C and the second peak around  $\sim 485$  °C. At present the reason for this is unknown.

### 3.4. Curing behaviour and glass transition study using DSC

#### 3.4.1. Curing behaviour

The curing behaviour of the UV curable polymer formulations was also found to influence the printing process and the final material properties. Fast curing of the material was predicted to contribute to improved print quality, resolution, and ease of fabrication of self-supported structures [42]. Furthermore, the degree of cure achieved during the reaction was also expected to influence the properties of the cross-linked polymer network, for example excess unreacted monomer may act as a plasticiser, or low cure may result in a lower branching density.

To characterise the curing behaviour, DSC analysis was conducted. Fig. 6 presents the UV-DSC heat flow curves as a function of time for five different uncured silicone samples. Negative values were observed for the heat flow, indicating that the chain polymerisation of C=C bonds in the (meth)acrylate groups was exothermic, as would be expected. This is a consequence of the conversion of  $\pi$ -bonds in the monomer into  $\sigma$ -bonds in the polymer after curing [49].

The reaction enthalpy  $\Delta H$  can be obtained via integration of the heat flow per unit mass with respect to time, see Fig. 7. The degree of cure  $\alpha_c$  can be determined from the ratio of the reaction enthalpy  $\Delta H$  to the total enthalpy of the reaction of the acrylate and methacrylate groups  $\Delta H_0$  [52,53] using

$$\alpha_c = \frac{\Delta H}{\Delta H_0} \quad (5)$$

where  $\Delta H_0$  is determined from the relationship

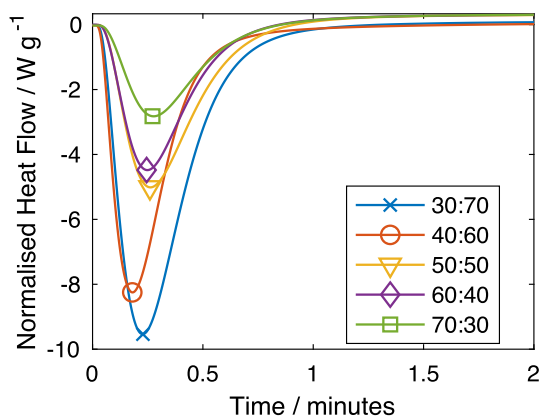


Fig. 7. Normalised heat flow versus time for various silicone:acrylate ratios.

Table 2

The mass ratio of PDMS-DMA in the mixture  $r$ , the reaction enthalpy  $\Delta H$ , the total enthalpy  $\Delta H_0$ , the experimentally measured ( $\alpha_{c,expt}$ ) and the molar corrected ( $\alpha_{c,corr}$ ) degree of cure for the various silicone:acrylate compositions considered.

Composition	$r$	$\Delta H / \text{J g}^{-1}$	$\Delta H_0 / \text{J g}^{-1}$	$\alpha_{c,expt} / \%$	$\alpha_{c,corr} / \%$
30:70	0.3	-215.0	-327.7	65.6%	65.7%
40:60	0.4	-150.0	-281.4	53.3%	53.4%
50:50	0.5	-133.0	-235.0	56.6%	56.8%
60:40	0.6	-111.0	-188.7	58.8%	59.1%
70:30	0.7	-85.0	-142.4	59.7%	60.2%

$$\Delta H_0 = (1 - r) \left[ \frac{\Delta H_0^{\text{EHA}}}{M^{\text{EHA}}} \right] + 2r \left[ \frac{\Delta H_0^{\text{PDMS-DMA}}}{M_{\text{n}}^{\text{PDMS-DMA}}} \right] \quad (6)$$

where  $\Delta H_0^{\text{EHA}}$  is equal to  $86 \text{ kJ mol}^{-1}$ ,  $\Delta H_0^{\text{PDMS-DMA}}$  is  $54.4 \text{ kJ mol}^{-1}$  and  $r$  is the mass ratio of the PDMS-DMA in the mixture. Additionally, since the PDMS has two methacrylate groups per molecule a factor of 2 is present outside the second square bracket [54,55].

Table 2 presents the calculated values for  $r$ ,  $\Delta H$ ,  $\Delta H_0$ ,  $\alpha_c$  and the molar corrected degree of cure  $\alpha_{c,corr}$  for the various silicone:acrylate compositions considered in this study.  $\alpha_{c,corr}$  is determined in a similar fashion to  $\alpha_c$  and differs only by the fact that a factor of 2 is not present outside the second square bracket in Eq. (6). The data shows that the greater the silicone content in the sample, the smaller the exothermic peak. This was attributed to: (a), the limitation in radial diffusion caused by an increase in viscosity of samples with higher silicone content and; (b), the overall reduction in methacrylate functional groups present due to the larger molecular weight of the silicone reagent. Furthermore, the data in Table 2 shows that the conversion of acrylate bonds is similar in all of the samples, once the difference in molecular weight is taken into account, and reaches around 60% at completion. Interestingly, most of the reaction was completed after  $\sim 30$  s. Thus, these results suggest that any observed changes in mechanical properties for different compositions will arise from differences in crosslink density within the cured material.

#### 3.4.2. Post-cure thermal properties

Additional DSC tests were conducted to attempt to determine the glass transition temperatures of the cured compositions. The transition temperatures were obtained from the peaks in the derivatives of the DSC count vs temperature curves, which are provided in the supplementary section (Fig. S6). The transition temperatures identified from these curves are shown on Fig. 8.

Each composition exhibits two distinct glass transitions, and hence the measurements confirm that there are two distinct sepa-

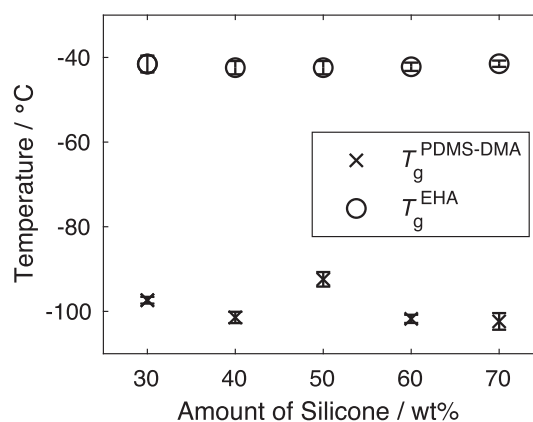
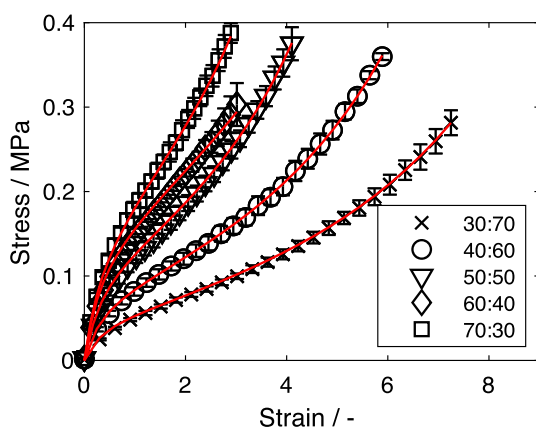


Fig. 8. The glass transition temperatures obtained for the various silicone:acrylate systems explored in the study.

rate phases. The lower glass transition temperature, circa  $-100\text{ }^{\circ}\text{C}$  was attributed to the silicone, whilst the higher, at around  $-43\text{ }^{\circ}\text{C}$  can be associated with the acrylate. Both appear to be approximately independent of the ratio of the components. Thus, this data suggests that the fully cured materials exist as phase separated structures in which there are domains of polymerised EHA and polymerised PDMS-DMA. Typical glass transition temperatures for polymerised EHA and PDMS have been reported as  $-50\text{ }^{\circ}\text{C}$  and  $-125\text{ }^{\circ}\text{C}$ , respectively [56,57]. The observed discrepancy between the transition temperatures of the distinct phases and the pure polymers could be attributed to factors including, but not limited to, the instrument of choice, the heating/cooling rates and the molecular weight, but is unlikely to be associated with

the degree of phase separation as no effect of component ratio was observed.

Further support of the existence of a phase separated structure is presented in the supplementary section (Figs. S7-S11), where similarities between the TGA decomposition profile of the compositions and the profiles produced from the individual components scaled by the corresponding mass ratios are shown [58]. The final product structure will be a result of a combination of both, tendency for these formulations to rapidly phase separate during curing and fast reaction kinetics of EHA. The reaction kinetics of the EHA monomer is expected to be faster than PDMS-DMA, due to the steric bulk of both the full monomer structure and that around the reacting radical centre. Thus, the final structure will take the form of very lightly cross linked or thermoplastic EHA regions existing in conjunction with heavily branched/crosslinked PDMS-DMA domains. The observations from the subsequent swelling experiments (Fig. 5) conducted on cured specimens indicated that there are no thermoplastic EHA regions as no part of the material structure was observed to dissolve out. It is concluded that an extended three-dimensional network has been created by cross-links between the surface of the domains and the matrix polymer.



**Fig. 9.** Average stress-strain response (symbols) of different compositions of cured silicone:acrylate systems obtained using the SER3-P. Error bars represent  $\pm 2$  standard errors. The data is limited to the lowest recorded failure strain in each batch of tests. An Edward Vilgis model is fitted to the experimental results to probe the changes in the elastomeric network (lines).

### 3.5. Mechanical properties and modelling

The average uniaxial tensile stress-strain responses obtained from a minimum of three specimens per sample for all the silicone:acrylate systems explored in this study are illustrated in Fig. 9, and the error bars represent  $\pm 2$  standard deviations. A table of tensile properties has been presented in the supplementary section, see Table S1.

Fig. 9 confirms that an excellent level of repeatability was achieved. The average curves are limited to the lowest failure strain recorded in each batch of samples. It is apparent that increasing the proportion of silicone leads to a stiffer response, as would be expected with greater levels of crosslinking, but at the

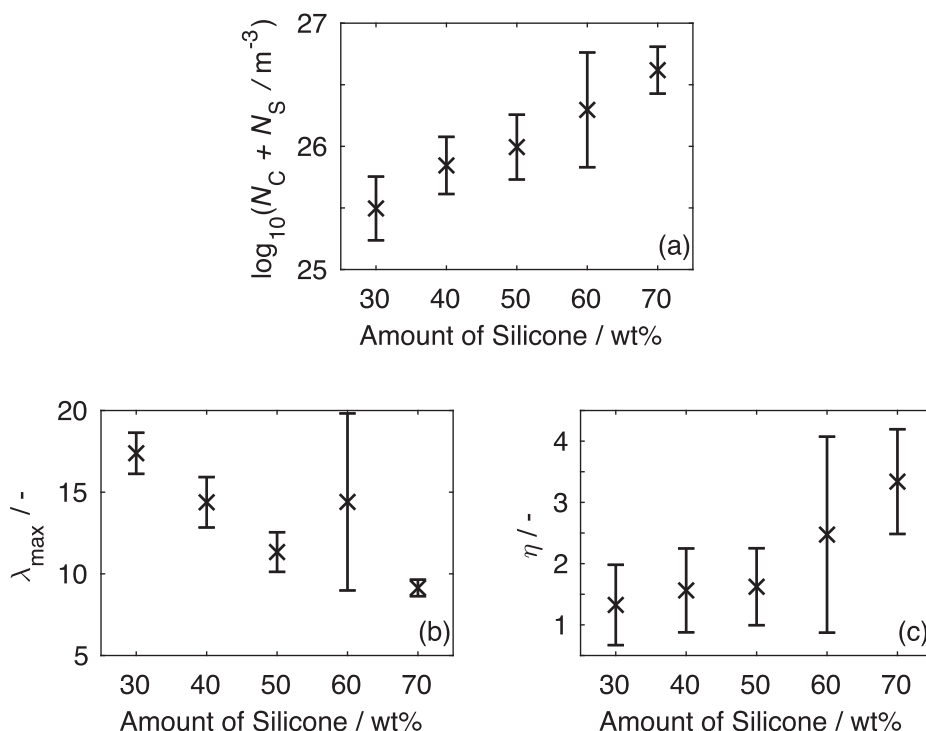


**Fig. 10.** (a) The network density, expressed as  $N_C + N_S$ , (b) the limiting extensibility of the network,  $\lambda_{max}$ , which is obtained from the inverse of the model parameter  $\alpha$ , and (c) the slip-link mobility  $\eta$ , all  $\pm 2$  standard deviations and shown as a function of composition.

expense of a reduction in the failure strain. To quantify the observed changes in the mechanical response with composition, a rubber model was fitted to the data. Although there are numerous applicable models in the literature, an Edwards-Vilgis (EV) model was selected due to the physical origin of its parameters [44]. Like many of the rubber models in literature, the EV model is intended for homogenous elastomers. Nonetheless, such models are frequently employed to successfully model the behaviour of heterogenous and filled elastomer systems, although interpretation of the parameters becomes more challenging. The strain energy function of the EV model has the form:

$$W = \frac{1}{2} N_C k_B T \left\{ \sum_{i=1}^3 \frac{\lambda_i^2 (1-\alpha^2)}{1-\alpha^2 \sum_{i=1}^3 \lambda_i^2} + \log \left( 1 - \alpha^2 \sum_{i=1}^3 \lambda_i^2 \right) \right\} + \frac{1}{2} N_S k_B T \sum_{i=1}^3 \left[ \left\{ \frac{\lambda_i (1+\eta)(1+\alpha^2)}{(1+\eta\lambda_i^2)(1-\alpha^2 \sum_{i=1}^3 \lambda_i^2)} + \log(1 + \eta\lambda_i^2) \right\} + \log(1 - \alpha^2 \sum_{i=1}^3 \lambda_i^2) \right] \quad (7)$$

where  $k_B$  is Boltzmann's constant,  $T$  is the absolute temperature,  $N_C$  is the cross-link density,  $N_S$  is the slip-link density,  $\eta$  is a measure of slip-link mobility,  $\alpha$  is a measure of finite chain extensibility and  $\lambda_i$  are the principal stretches. The slip-links are a simplification of the entanglement constraints observed in real polymer systems.

Assuming isochoric deformation during the uniaxial tensile tests, the principal stretches are given by  $\lambda_1 = \lambda$  and  $\lambda_2 = \lambda_3 = \lambda^{-1/2}$ , where  $\lambda$  is the tensile stretch imposed on the specimen during the test [59]. The stress is obtained by applying these to Eq. (7), and differentiating with respect to  $\lambda$ . Model parameters were obtained by minimising the root-mean-square (RMS) error between the experimental and model stress using the MATLAB *lsqcurvefit* function. In all cases, the EV function provided an excellent fit to the experimental data with RMS errors not exceeding 1.8 kPa. The evolution of the EV model parameters is shown in Fig. 10 as a function of the composition.

As the EV function is relatively insensitive to the split between cross-links and slip-links, Fig. 10a reports the total  $N_S + N_C$ , which can be observed to increase systematically with increasing silicone content. This is attributed to the ability of the two methacrylate end groups of the PDMS to form cross-links with the monoacrylate chains. An increase in cross-link density can also lead to an increase in the entanglement density, as there is a greater likelihood of trapped entanglements being present between cross-links [59]. The network densities of the different compositions were also determined on the basis of the swelling study, resulting in  $\log_{10}(N_S + N_C)$  values ranging between 25.4 and 25.7 as the silicone content is increased from 30 to 70 wt%. The corresponding calculations have been provided in the supplementary material. Although the change in network density with composition measured through swelling is more limited than that observed in the EV model, the trends are similar.

Fig. 10b shows the limiting extensibility of the network,  $\lambda_{max}$ , which is obtained from the inverse of the model parameter  $\alpha$ . In line with the network density, the limiting extensibility decreases with increasing silicone content, except for the 60:40 composition, where the determination of the limiting extensibility was hampered by a more limited dataset due to failure of the specimens at reduced strains. Nevertheless, overall, as the density of network constraints increases, the chain length between these constraints decreases, leading to a reduction in the limiting elongation. Lastly, Fig. 10c shows that the slip-link mobility increases with increasing silicone content, most likely attributed to the greater flexibility of the silicone chains relative to the acrylate chains.

By expressing the evolution of EV parameters as simple functions of composition, a predictive model can be deployed as a tool to enable the fine tuning of properties for various applications. As an illustration, Fig. 11 shows the measured ( $\pm 3$  standard deviation)

and model derived secant modulus  $E_{s,100\%}$ , a value typically quoted in material data sheets.  $E_{s,100\%}$  has also been included in the table of tensile properties provided in the supplementary section, see Table S1. An increase in silicone content from 30 to 70 wt% increases  $E_{s,100\%}$  by a factor of  $\sim 3.6$ . Thus, this demonstrates that this model provides a fair prediction of the experimental data. Lastly, as evidenced by the low modulus, it is apparent that these materials are not intended as substitutes for classical silicone elastomer. Nevertheless, materials such as these are well suited for applications where soft elastomers with complex geometries are required, such as in soft robotics.

### 3.6. Validation of 3D printing capability

The custom material jetting apparatus described in Section 2.5 was utilised to showcase how the formulation could be used to 3D print arbitrary shapes. An example of a successfully printed silicone sample of the 70:30 composition is shown in Fig. 12.

On closer inspection it can be observed that the surface is not completely smooth and air bubbles are present. Whilst material and process optimisation is still required, Fig. 12 shows the ability to use these formulations for 3D printing.

These initial trials have shown that this family of flexible, tuneable materials can be used in 3D printing. The formulation strategy employed, in one step, creates a phase separated, lightly cross-linked structure. Considerations for future work will focus on the further printing process optimisation, and demonstrating the capability to produce 3D structures with locally tuned mechanical properties varying across all three dimensions by using multiple nozzles.

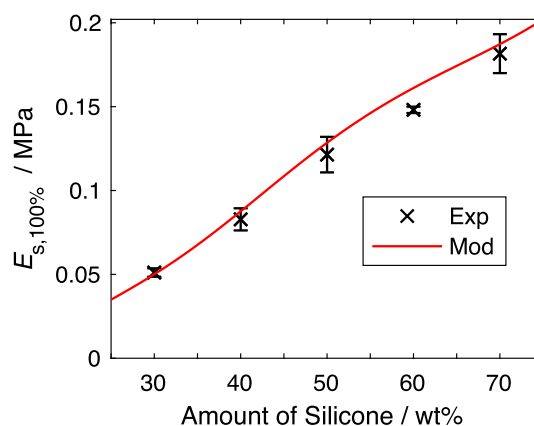


Fig. 11. The experimentally measured (symbols) ( $\pm 3$  standard errors) and the secant modulus  $E_{s,100\%}$  predicted from the model (line) as a function of composition.

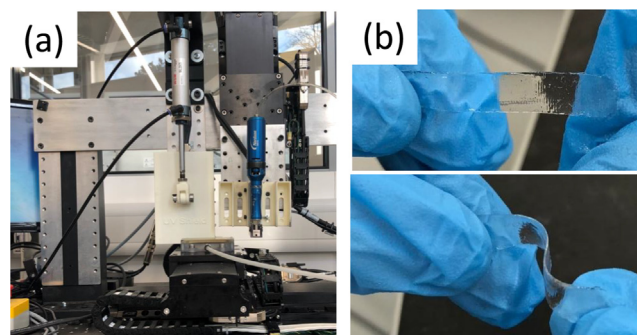


Fig. 12. (a) The custom jetting setup used for 3D printing and (b) a printed 70:30 sample.

#### 4. Conclusions

In this work, we have reported the creation of a family of novel UV-curable, highly flexible silicone compositions which are suitable for use in a valve-based jetting process. Furthermore, the design of these formulation successfully exploits the balance between in-cure phase separation and differential reactivity to produce composites structures with tuneable materials properties. Property tuning is achieved by simply varying the ratio of the polymerisable regents within the formulation. Thus, taking advantage of multiple jetting heads and correlation between the material composition and mechanical properties, it might be possible to fabricate functional devices with locally tuned, highly flexible mechanical properties *via* 3D printing. However, more tests are required to make sure that different silicone:acrylate ratios are interfaceable. The formulation strategy is proposed to create a highly phase separated, lightly crosslinked structures that delivers the beneficial material properties by jointly inspiring and limiting the crosslink levels achieved and variability is created by the relative domain: matrix ratio.

The FTIR spectra of the samples before and after curing confirmed successful crosslinking reactions within all the compositions. The DSC study showed that the reaction rate varied from composition to composition as expected due to the differentiated reactivity of the two polymerisable components. However, this had no discernible impact on the overall time of the reaction, which remained within 30 s to reach the maximum cure level. The conversion of the C=C double bond reached ~60% for all of the samples, indicating that the observed changes in mechanical properties results from difference in crosslinking density. The presence of two distinct glass transitions was observed during DSC tests indicating that the sample is phase-separated into silicone and acrylate phases. The TGA study demonstrated the first decomposition peak was observed to be similar for all composition and it was ~420 °C.

The results from the mechanical tests suggest that varying the silicone content results in a systematic variation in the stress-strain response. An EV model was fitted to the experimental data to study this variation. The network density is seen to grow with increasing silicone content due to the higher number of available reaction sites. This shortens the chain length, and hence the limiting extensibility is seen to drop. The increase in slip-link mobility with silicone content is attributed to the greater flexibility of the silicone molecule. It was shown that the model could be helpful in tuning the mechanical properties of this particular group of materials. A more detailed investigation into the mechanical properties will be required prior to application in the aforementioned applications, in particular the reversibility of the mechanical response, and the resistance to crack propagation. Lastly, an initial assessment was performed to validate the 3D printing capability of these materials, and results indicate that the material is printable. The work opens a possibility of employing developed silicone:acrylate formulations for producing 3D structures with locally tuned mechanical properties within the same material. The novel UV-cured silicone materials are softer than the classical platinum-catalyzed addition cured PDMS materials, and will be of particular interest in applications such as soft robotics, where soft elastomers with complex geometries are required.

#### Declaration of Competing Interest

The authors declare that they have no known competing financial interests or personal relationships that could have appeared to influence the work reported in this paper.

#### Acknowledgements

This work was supported by AWE Plc., Aldermaston, Reading, United Kingdom.

We thank Dr Yinfeng He for his help with TGA decomposition profile analysis.

#### Appendix A. Supplementary material

Supplementary data to this article can be found online at <https://doi.org/10.1016/j.matdes.2021.109681>.

#### References

- [1] A. Debelle, L. Hermans, M. Bosquet, S. Dehaeck, L. Lonys, B. Scheid, et al., Soft encapsulation of flexible electrical stimulation implant: challenges and innovations, *Eur. J. Transl. Myol.* (2016).
- [2] A. Abbad, K. Jaboviste, M. Ouisse, N. Dauchez, Acoustic performances of silicone foams for sound absorption, *J. Cell. Plast.* (2018).
- [3] H. Khan, M. Amin, A. Ahmad, Characteristics of silicone composites for high voltage insulations, *Rev. Adv. Mater. Sci.* (2018).
- [4] E. Delebecq, N. Hermeline, A. Flers, F. Ganachaud, Looking over liquid silicone rubbers: (2) Mechanical properties vs network topology, *ACS Appl. Mater. Interfaces* (2012).
- [5] F. Schmitt, O. Piccin, L. Barbé, B. Bayle, Soft robots manufacturing: a review, *Front. Robotics AI* (2018).
- [6] Y. Poojari, Silicones for encapsulation of medical device implants, *Silicon* (2017).
- [7] M. Cai, S. Nie, Y. Du, C. Wang, J. Song, Soft elastomers with programmable stiffness as strain-isolating substrates for stretchable electronics, *ACS Appl. Mater. Interfaces* (2019).
- [8] K. Goswami, A.L. Skov, A.E. Daugaard, UV-cured, platinum-free, soft poly (dimethylsiloxane) networks, *Chem. - A Eur. J.* (2014).
- [9] A.S. Fawcett, M.A. Brook, Thermoplastic silicone elastomers through self-association of pendant coumarin groups, *Macromolecules* (2014).
- [10] A.S. Fawcett, T.C. Hughes, L. Zepeda-Velazquez, M.A. Brook, Phototunable cross-linked polysiloxanes, *Macromolecules* (2015).
- [11] F.B. Madsen, L. Yu, A.L. Skov, Self-healing, high-permittivity silicone dielectric elastomer, *ACS Macro Lett.* (2016).
- [12] T.J. Hinton, Q. Jallerat, R.N. Palchesko, J.H. Park, M.S. Grodzicki, H.J. Shue, et al., Three-dimensional printing of complex biological structures by freeform reversible embedding of suspended hydrogels, *Sci. Adv.* (2015).
- [13] L. Low, S. Ramadan, C. Coolens, H.E. Naguib, 3D printing complex lattice structures for permeable liver phantom fabrication, *Bioprinting.* (2018).
- [14] Z. Zhao, X. Kuang, J. Wu, Q. Zhang, G.H. Paulino, H.J. Qi, et al., 3D printing of complex origami assemblages for reconfigurable structures, *Soft Matter* (2018).
- [15] E. Fantino, A. Chiappone, I. Roppolo, D. Manfredi, R. Bongiovanni, C.F. Pirri, et al., 3D printing of conductive complex structures with in situ generation of silver nanoparticles, *Adv. Mater.* 28 (19) (2016) 3712–3717.
- [16] C. Hopmann, A. Funk, C. Windeck, Investigations on the processing of solid silicon rubber in blow moulding, *AIP Conf. Proc.* (2015).
- [17] F.Y. Su, X.Q. Wu, Experimental study on silicone rubber mold design for thermal expansion RTM, *J. Reinf. Plast. Compos.* (2010).
- [18] C. Hopmann, M. Röbig, High precision optics for LED applications made of liquid silicone rubber (LSR), in: *Progress in Rubber, Plastics and Recycling Technology*, 2017.
- [19] Y. Wang, C. Gregory, M.A. Minor, Improving mechanical properties of molded silicone rubber for soft robotics through fabric compositing, *Soft Robot.* (2018).
- [20] M. Schaffner, J.A. Faber, L. Pianegonda, P.A. Rühs, F. Coulter, A.R. Studart, 3D printing of robotic soft actuators with programmable bioinspired architectures, *Nat. Commun.* (2018).
- [21] M.S. Mannoor, Z. Jiang, T. James, Y.L. Kong, K.A. Malatesta, W.O. Soboyejo, et al., 3D printed bionic ears, *Nano Lett.* (2013).
- [22] E.B. Duoss, T.H. Weisgraber, K. Hearon, C. Zhu, W. Small IV, T.R. Metz, et al., Three-dimensional printing of elastomeric, cellular architectures with negative stiffness, *Adv. Funct. Mater.* (2014).
- [23] F. Liravi, R. Darleux, E. Toyserkani, Nozzle dispensing additive manufacturing of polysiloxane: dimensional control, *Int. J. Rapid Manuf.* (2015).
- [24] D.B. Kolesky, R.L. Truby, A.S. Gladman, T.A. Busbee, K.A. Homan, J.A. Lewis, 3D bioprinting of vascularized, heterogeneous cell-laden tissue constructs, *Adv. Mater.* (2014).
- [25] D.B. Kolesky, K.A. Homan, M.A. Skylar-Scott, J.A. Lewis, Three-dimensional bioprinting of thick vascularized tissues, *Proc. Natl. Acad. Sci. USA* (2016).
- [26] K. Tian, J. Bae, S.E. Bakarich, C. Yang, R.D. Gately, G.M. Spinks, et al., 3D printing of transparent and conductive heterogeneous hydrogel-elastomer systems, *Adv. Mater.* (2017).

- [27] A.M. Schmalzer, C.M. Cady, D. Geller, D. Ortiz-Acosta, A.T. Zocco, J. Stull, et al., Gamma radiation effects on siloxane-based additive manufactured structures, *Radiat. Phys. Chem.* (2017).
- [28] T.J. Hinton, A. Hudson, K. Pusch, A. Lee, A.W. Feinberg, 3D printing PDMS elastomer in a hydrophilic support bath via freeform reversible embedding, *ACS Biomater. Sci. Eng.* (2016).
- [29] X. Cui, T. Boland, D.D.K. D'Lima, M. Lotz, Thermal inkjet printing in tissue engineering and regenerative medicine, *Recent Pat. Drug Deliv. Formul.* (2012).
- [30] B. Derby, Additive manufacture of ceramics components by inkjet printing, *Engineering* (2015).
- [31] H. Yang, Y. He, C. Tuck, R. Wildman, I. Ashcroft, P. Dickens, et al., High viscosity jetting system for 3D reactive inkjet printing, in: 24th International SFF Symposium - An Additive Manufacturing Conference, SFF 2013, 2013.
- [32] A. Foerster, R. Wildman, R. Hague, C. Tuck, A. Terry, Development of 3D cellular silicone structures using reactive inkjet printing approach for energy absorbing application, in: *Syntactic Compos Foam V*, 2017.
- [33] E. Selbertinger, F. Achenbach, B. Pachaly, Method for producing silicone elastomer parts. US20170312981A1, 2014.
- [34] F. Liravi, R. Darleux, E. Toyserkani, Additive manufacturing of 3D structures with non-Newtonian highly viscous fluids: finite element modeling and experimental validation, *Addit. Manuf.* (2017).
- [35] D.S. Kim (Danny), B.L. Tai, Hydrostatic support-free fabrication of three-dimensional soft structures, *J. Manuf. Process.* (2016).
- [36] C.S. O'Bryan, T. Bhattacharjee, S. Hart, C.P. Kabb, K.D. Schulze, I. Chilakala, et al., Self-assembled micro-organogels for 3D printing silicone structures, *Sci. Adv.* (2017).
- [37] V. Shastri, Non-Degradable biocompatible polymers in medicine: past: present and future, *Curr. Pharm. Biotechnol.* (2005).
- [38] C. Sturgess, C.J. Tuck, I.A. Ashcroft, R.D. Wildman, 3D reactive inkjet printing of polydimethylsiloxane, *J. Mater. Chem. C* (2017).
- [39] D.A. Porter, A.L. Cohen, P.S. Krueger, D.Y. Son, Additive manufacturing with ultraviolet curable silicones containing carbon black, *3D Print Addit Manuf.* (2018).
- [40] D.T. Kuhnel, J.M. Rossiter, C.F.J. Faul, 3D printing with light: towards additive manufacturing of soft, electroactive structures, 2018.
- [41] D.K. Patel, A.H. Sakhaei, M. Layani, B. Zhang, Q. Ge, S. Magdassi, Highly stretchable and UV curable elastomers for digital light processing based 3D printing, *Adv. Mater.* (2017).
- [42] Y. He, C.J. Tuck, E. Prina, S. Kilsby, S.D.R. Christie, S. Edmondson, et al., A new photocrosslinkable polycaprolactone-based ink for three-dimensional inkjet printing, *J. Biomed. Mater. Res. - Part B Appl. Biomater.* 105 (6) (2017) 1645–1657.
- [43] D.S. Kim (Danny), Y.T. Kao, B.L. Tai, Hydrostatic 3D-printing for soft material structures using low one-photon polymerization, *Manuf Lett.* (2016).
- [44] S.F. Edwards, T. Vilgis, The effect of entanglements in rubber elasticity, *Polymer (Guildf)*. 27 (4) (1986) 483–492.
- [45] J. Fahrenfort, Attenuated total reflection. A new principle for the production of useful infra-red reflection spectra of organic compounds, *Spectrochim. Acta* (1961).
- [46] J.P. Fisher, T.A. Holland, D. Dean, A.G. Mikos, Photoinitiated cross-linking of the biodegradable polyester poly(propylene fumarate). Part II. In vitro degradation, *Biomacromolecules* (2003).
- [47] S. Tanodekaew, S. Channasanon, P. Uppanan, Xylan/polyvinyl alcohol blend and its performance as hydrogel, *J. Appl. Polym. Sci.* 100 (3) (2006) 1914–1918.
- [48] N.N. Lebedev, I.S. Ufliand, Axisymmetric contact problem for an elastic layer, *J. Appl. Math. Mech.* 22 (3) (1958) 442–450.
- [49] R.V. Ghorpade, S.M. Bhosle, S. Ponrathnam, C.R. Rajan, N.N. Chavan, R. Harikrishna, Photopolymerization kinetics of 2-phenylethyl (meth) acrylates studied by photo DSC, *J. Polym. Res.* (2012).
- [50] H. Wang, W. Liu, Z. Yan, J. Tan, G. Xia-Hou, Synthesis and characterization of UV-curable acrylate films modified by functional methacrylate terminated polysiloxane hybrid oligomers, *RSC Adv.* (2015).
- [51] E. Oglioni, L. Yu, P. Mazurek, A.L. Skov, Designing reliable silicone elastomers for high-temperature applications, *Polym. Degrad. Stab.* (2018).
- [52] A. Palanisamy, B.S. Rao, Photo-DSC and dynamic mechanical studies on UV curable compositions containing diacrylate of ricinoleic acid amide derived from castor oil, *Prog. Org. Coat.* (2007).
- [53] H.D. Hwang, C.H. Park, J.I. Moon, H.J. Kim, T. Masubuchi, UV-curing behavior and physical properties of waterborne UV-curable polycarbonate-based polyurethane dispersion, *Prog. Org. Coat.* (2011).
- [54] K.S. Anseth, C.N. Bowman, N.A. Peppas, Polymerization kinetics and volume relaxation behavior of photopolymerized multifunctional monomers producing highly crosslinked networks, *J. Polym. Sci., Part A: Polym. Chem.* (1994).
- [55] X. Jiang, H. Xu, J. Yin, Polymeric amine bearing side-chain thioxanthone as a novel photoinitiator for photopolymerization, *Polymer (Guildf)* (2004).
- [56] M.H. Keshavarz, K. Esmailpour, H. Taghizadeh, A new approach for assessment of glass transition temperature of acrylic and methacrylic polymers from structure of their monomers without using any computer codes, *J. Therm. Anal. Calorim.* (2016).
- [57] N. Bosq, N. Guigo, J. Persello, N. Sbirrazzuoli, Melt and glass crystallization of PDMS and PDMS silica nanocomposites, *PCCP* (2014).
- [58] D.J. Haloi, B.P. Koiry, P. Mandal, N.K. Singha, Synthesis and characterization of poly(2-ethylhexyl acrylate) prepared via atom transfer radical polymerization, reverse atom transfer radical polymerization and radical polymerization, *J. Chem. Sci.* 125 (4) (2013) 791–797.
- [59] L.R.G. Treloar, *The Physics of Rubber Elasticity*. OUP Oxford, 2005. (Oxford Classic Texts in the Physical Sciences).